ACS APPLIED NANO MATERIALS

www.acsanm.org Article

Transparent Glass Surfaces with Silica Nanopillars for Radiative Cooling

Javier Arrés Chillón, Bruno Paulillo,* Prantik Mazumder, and Valerio Pruneri*

Cite This: *ACS Appl. Nano Mater.* 2022, 5, 17606−17612 Read Online

ACCESS | Metrics & More | Article Recommendations | Supporting Information

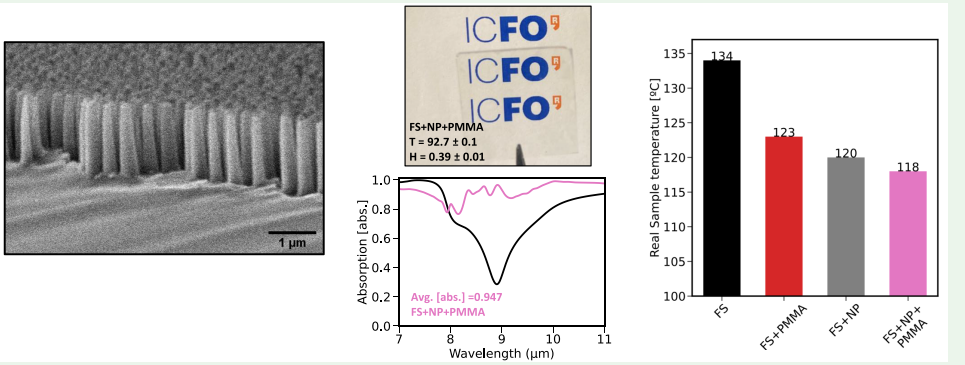

ABSTRACT: The increasing global use of cooling systems and the need of reducing greenhouse effect are pushing the emergence of more efficient cooling methods. In particular, passive radiative cooling technology extracts heat from objects by tailoring their optical emissivity using surface micro- and nanostructuring. Being capable of increasing thermal emissivity is especially relevant for widespread glass structures and devices, e.g., displays, car and building windows, and solar cells. In this paper, we propose a scalable lithography-free nanostructuring method to increase the infrared (IR) emissivity of glass by reducing the high reflection associated with the SiO_2 Reststrahlen band around 9 μm wavelength. Furthermore, we show that with an additional thin polymer coating the scattering (haze) in the visible due to the deep nanostructures can be dramatically reduced while maintaining the large IR emissivity. We experimentally prove that our nanostructured surface can extract more heat via radiation emission than the bare glass substrate, while keeping full transparency.

KEYWORDS: *glass nanostructures, radiative cooling, thermal radiation, scalable nanostructures, transparent surfaces*

INTRODUCTION

Today, cooling technologies represent 16% of household energy consumption[1] and contribute to 10% of global greenhouse emissions.[2] More efficient cooling technologies are desired toward the goal of net zero emissions by 2050, especially for widespread consumer electronics (e.g., displays and solar cells) to counteract device heating. While active cooling systems such as fans or liquid cooling are effective, they also increase size, weight, cost, and power consumption of the devices.

Recently, alternative and more efficient cooling methods that do not require external energy consumption have been studied.[3] One of these methods is passive radiative cooling (PRC), which extracts heat from bodies by tailoring the optical emissivity.[4] This method relies on increasing the emissivity of objects in the wavelength range between 8 and 13 μm, where the atmosphere transparency window (ATW) is located, thereby facilitating radiation of heat toward the outer space, meanwhile keeping low optical absorption in the visible and near-IR regions to avoid heating.

Dielectric/metal multilayer coatings[5−10] and periodic or random distribution of micro/nano structures supporting surface phonon polariton (SPhP) excitations[11−17] on a surface were proposed to increase the emissivity in the ATW. Porous surfaces[18−23] and paints[24,25] are additional examples of randomly distributed elements for PRC. Although these designs are optimized for PRC applications, most of them are related to surfaces that present a color, scatter and/or have a high reflectivity in the visible range, these properties being incompatible with displays and other applications where transparency (i.e., neutral color transmission and low haze) is a requirement.

Received: July 26, 2022
Accepted: October 20, 2022
Published: December 5, 2022

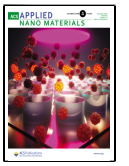

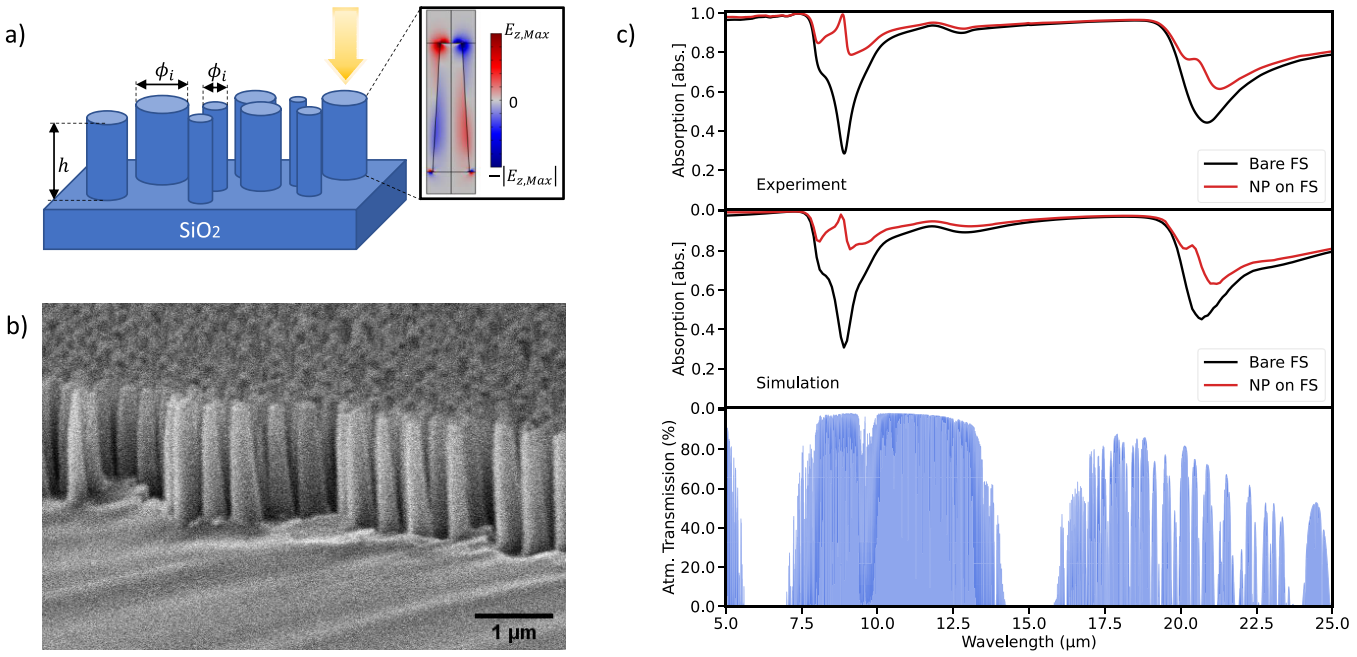

Figure 1. Nanostructured glass for radiative cooling. (a) Left: schematics of the proposed surface made of nanopillars (NPs) with height h and average diameter $\phi_{AVG} = \langle \phi_i \rangle$. Right: simulated electric field distribution in the NP at 9 μm. (b) SEM image of a typical NP surface structure with $h \approx 1250$ nm and $\phi_{Tip-AVG} = 172$ nm. (c) Top panel: experimental optical absorption spectra of flat FS (black line) and randomly distributed NPs on FS (red line) in the IR optical range. Middle panel: simulated optical absorption spectra of flat FS (black line) and a perfect array of NPs (red line) with $h = 1250$ nm, $\phi_{Bottom} = 307$ nm, $\phi_{Top} = 172$ nm, and $P = 410$ nm. Bottom panel: atmospheric optical transmission in the IR optical range (from 5 to 25 μm).[35]

Polymer coatings have also been widely used for PRC[9,18,21,26,27] because their molecular vibrational bands fall in the mid-IR range, thus increasing the emissivity in the ATW while having low light absorption in the visible and near-IR ranges.

Devising surfaces with radiative cooling properties is particularly relevant for widespread glass devices such as displays, windshields,[28] and smart windows[29] due to the fact that SiO_2 strongly reflects IR radiation emitted by the objects at room temperature (i.e., around 9 μm wavelength) because of its phonon modes,[30−32] which significantly decreases glass emissivity.

In this paper, we introduce a new type of surface for PRC based on scalable fabrication of nanopillars (NPs) on glass (e.g., fused silica (FS)). The proposed nanostructure reduces the Reststrahlen band of SiO_2 located near 9 μm wavelength by coupling light with SPhP modes.[11,14] In addition, we show that a thin polymer coating embedding the NPs can remove the haze produced by the nanostructure in the visible optical range, increasing the transmission and allowing this design for optical screens applications. Lastly, we demonstrate that our design can extract more heat via radiation emission at a given temperature than a bare glass substrate.

EXPERIMENTAL SECTION

Electromagnetic Simulations. Electromagnetic simulations of the glass NPs optical response were performed using a Finite Elements Method commercial software (Comsol). The SiO_2 permittivity dispersion is taken from Kitamura et al.[30] A NP array unit cell is simulated using periodic boundary conditions, which corresponds to simulating an ideal periodic array. Note, however, that such a model can be used to predict the IR response of the fabricated random NPs, the NP surface being a highly subwavelength nanostructure (average distance between neighbor NPs $\ll$ IR wavelengths).

Fabrication. The fabrication of the NPs surfaces was performed following the process used in refs 33 and 34 which has been shown to be suitable for a size of at least 4 × 4 in.^{2}. Bare and nanostructured substrates used in this work were ultraviolet-grade fused silica (FS) glass, with 1 in. square area and 1 mm thickness. The samples were cleaned in two ultrasonic baths—first in acetone and second in isopropanol, each one for 5 min. After the second bath, the samples were dried first with nitrogen and then with an oxygen plasma cleaning (PVA TePla 300 SemiAuto Plasma Asher). For the plasma cleaning, the recipe used was for 5 min, with 700 W of power and 300 mL/min of O_2.

To fabricate the NP mask, first a sputtering deposition of 15 nm of Cu was done at working pressure $\approx 1.5 \times 10^{-3}$ Torr, 20 °C, 20 sccm of Ar, and 100 W of DC power, obtaining a deposition rate of ≈0.200 nm/s. Afterward, a rapid thermal annealing was done in a UniTemp RTP-150-HV system at 750 °C for 135 s. Before the annealing process, the samples were cleaned with a nitrogen air gun.

The NPs were created by reactive ion etching (RIE) process using a Plasmalab System 100 from Oxford Instruments. The RIE process was done with 300 W of RF power at 20 °C and 30 mTorr, with 15 sccm of CHF_3 and 40 sccm of Ar gas plasma. The height of the NPs can be tuned by changing the etching time. The dry etching process was followed by a chemical ammonium persulfate bath to remove the remaining Cu nanoparticles. The fabricated NP surfaces were later cleaned following the same process described above.

For the polymer coating, a solution of PMMA in anisole was used to help the PMMA filter between the NP structure, due to surface polarity. To create a smooth coating, a drop of the mixture was spin-coated first at 500 rpm with an acceleration of 100 rpm/s for 35 s and then at 4000 rpm with an acceleration of 500 rpm/s for 15 s. The same coating was done for the coated bare FS. After the coating process, the samples were heated at 95 °C on a hot plate for 5 min to remove the solvent.

Optical Characterization. The samples have been optically characterized to obtain direct transmission (normal angle of

https://doi.org/10.1021/acsanm.2c03272
ACS Appl. Nano Mater. 2022, 5, 17606−17612

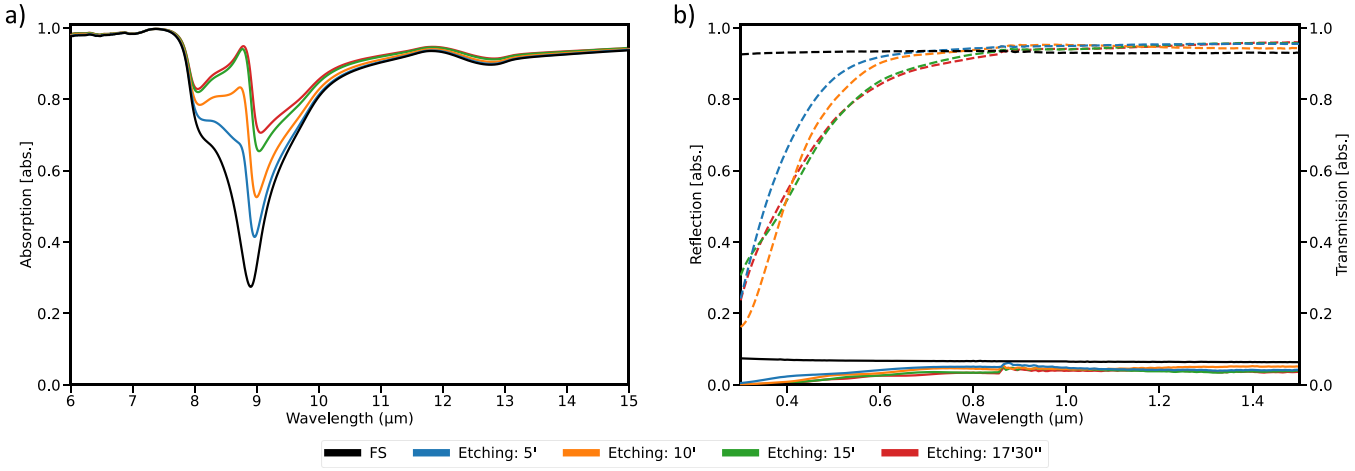

Figure 2. Effect of the NPs height on optical properties. (a) IR absorption for different etching times, i.e., different NPs heights. The larger the NPs, the larger is the splitting between the two phonon modes. Each etching time is represented with a different color. (b) Visible/near-IR optical response for different etching times. Continuous and dashed lines represent direct reflection and transmission, respectively. Note that reflection and transmission measurements are taken with the beam incident on the nanostructured surface.

incidence) and reflection at a quasi-normal angle (12°) of incidence using a Pelkin Elmer Lambda spectrometer in the 300 nm−1.5 μm wavelength range. For the 1.5−25 μm range, a Bruker Tensor FTIR was used, with reflection measurements at a quasi-normal angle (10°) of incidence. Specular reflection upon illumination at different angles of incidence was recorded using a Bruker A513/Q variable angle reflection accessory . We measured the reflection of the sample using the same incidence and detection angles ($\theta_{inc} = \theta_{det}$), ranging from 13° to 85°.

Samples haze and the corresponding total transmission are measured with a Labthink WGT-S haze meter, with a standard C light source. The total transmission is measured using an integration sphere, and the haze is a percentage from the incident light and the diffused light with an angle >2.5°. For all the measurements, an average and the corresponding statistical error value are obtained from five consecutive measurements.

IR Thermal Measurements. Thermal images have been taken using an Agilent TrueIR U5855A thermal camera, and the corresponding temperatures of the hot plate are measured with a thermocouple connected to a LabSmith 4AM01 analogue sensor manifold.

RESULTS AND DISCUSSION

Our design consists of randomly distributed NPs etched in FS substrate, as illustrated in Figure 1a. This nanostructured glass surface can reduce the Reststrahlen band of FS located around 9 μm wavelength by increasing its absorptivity (and, because of Kirchhoff's law, its emissivity) as confirmed by both experiments and electromagnetic simulations. The inset of Figure 1a shows the Z component of the electric field corresponding to a representative NP array. The dimensions of the NP structure used in the simulations are average experimental values estimated from scanning electron microscopy (SEM) images (see below). The evanescent electric field enhancement at the surface of the nanopillar proves the coupling between light and SPhP of SiO_2. This coupling increases the absorption of the surface at the Reststrahlen band.[14]

The SEM image in Figure 1b shows a typical fabricated NPs structure on glass. The average tip diameter is around 172 nm, about ≈60% of the base radius, with a filling area ratio (surface area filled by the nanostructure per unit area) of 14% (see the Supporting Information). From these values, the nanostructured surface can be approximated as a NP array with a period 410 nm. The nanopillars have an estimated height of 1250 nm.

Figure 1c, top and middle panels, shows the spectral optical absorption, $A = 1 - R - T$ (R as reflectance and T as transmittance, both direct), of bare FS (black lines) and FS +NP (red lines) in the IR optical range. In the mid-IR range, the NP dimensions are much smaller than the light wavelength, making scattering negligible. Therefore, transmission and reflection have only a direct contribution. The experimental results in the top panel agree well with the simulations of the middle panel. In the bottom panel the optical transmission of the atmosphere in the IR optical range is showed.[35] As it can be seen, the NPs on FS increase the emissivity of the glass substrate near the reflection band, allowing almost unit emissivity at ≈9 μm. The same effect is also observed in the second phonon band, located at ≈21 μm.

Next, we show how the optical reflection/absorption in the SiO_2 phonon band changes as a function of the surface geometry, namely the NP height, that is controlled by processing parameters. Figure 2a shows different NPs substrates prepared with the same Cu nanoparticle mask but etched for different times. A longer RIE time creates taller NPs, which leads to increased absorption (i.e., reduced reflection) in the SiO_2 Reststrahlen band, as investigated for similar nanostructures.[11,36] This experimental trend was also confirmed by the numerical study reported in the Supporting Information where the nanostructure response was explored as a function of the NP array geometrical parameters.

Simulations show that the higher the density and the larger the height of NPs, the greater the IR absorption in the ATW. However, due to our scalable fabrication method, a trade-off between the NP height and density exists because the geometrical parameters of the dewetted Cu nanoparticles mask (particle diameter, density/filling ratio, and metal thickness) determine the maximum NP height achievable by RIE. Hence, to obtain higher NPs, one would need a dewetted mask of larger Cu nanoparticles, which would lead to a lower density of NPs.

Note that such NPs strongly scatter in the visible wavelengths, making the sample surface visibly hazy. The values of the total transmission (T_{Tot}) and haze (H) of bare FS

https://doi.org/10.1021/acsanm.2c03272
ACS Appl. Nano Mater. 2022, 5, 17606−17612

Table 1. Optical Total and Averaged Direct Transmission and Haze for Bare FS and FS+NP with Different Etching Times, i.e., NP Heights

	FS	etching: 5 min	etching: 10 min	etching: 15 min	etching: 17 min 30 s
T_{Tot} (%)	93.1 ± 0.1	92.8 ± 0.1	93.1 ± 0.1	93.0 ± 0.0	93.6 ± 0.1
$T_{Dir\text{-}AVG}$ (%)	93.3 ± 0.1	83.7 ± 0.4	78.1 ± 2.3	74.8 ± 0.4	75.1 ± 0.7
haze (%)	0.04 ± 0.01	5.10 ± 0.13	11.77 ± 0.71	15.01 ± 0.79	15.46 ± 0.90

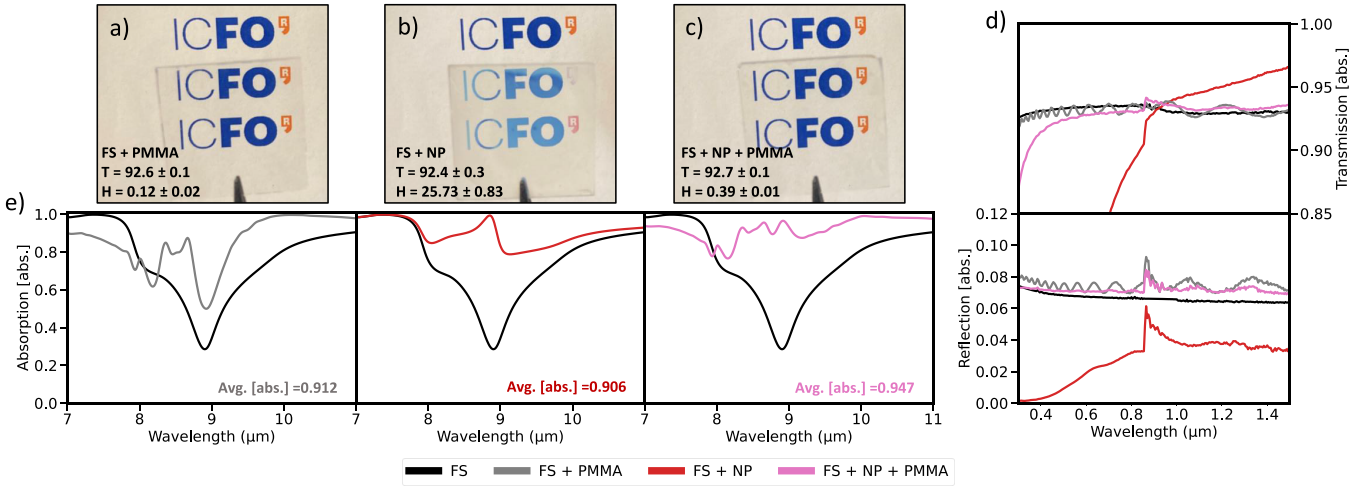

Figure 3. Effect of the nanopillar coating on the optical properties. (a–c) Photos of FS coated with PMMA, NP etched on FS, and NP etched on FS coated with PMMA, respectively. (d) Visible/near-IR optical response of bare FS and NP etched on FS with and without PMMA coating. Top/bottom plots represents direct transmission/reflection, respectively. (e) From left to right, IR absorption for FS coated with PMMA (gray line), NP etched on FS (red line), and NP etched on FS coated with PMMA (pink line). In each panel, the average absorption between 8 and 13 μm is shown. The black line shows absorption of bare FS, as reference. Note that reflection and transmission measurements are taken with the beam incident on the nanostructured surface.

and FS+NP surfaces with different etching times are reported in Table 1. T_{Tot} includes both direct and diffused contributions. Also, the averaged direct transmission ($T_{Dir\text{-}AVG}$) values in the 350 and 750 nm optical range from Figure 2a data are reported.

T_{Tot} is fairly constant for different nanopillar heights, while the haze increases, meaning that the optical absorption from the nanostructure is negligible. The increasing haze at short wavelengths can also be seen in the spectra of Figure 2b, where the visible direct reflection (continuous lines) and transmission (dashed lines) measured decrease as a function of RIE time, for the samples of Table 1. Here, one can see that both direct transmission and reflection drop approaching the UV region due to the increased surface scattering, while the absorption from the NP surface is negligible ($R_{Dir} + T_{Dir} + A + S = 1$, with $A \approx 0$). S includes both diffused transmission and reflection.

A large NP height is desirable for increasing glass absorption and suppressing reflection close to the 9 μm SiO_2 phonon band. However, this increases the haze in the visible range, giving the samples a bluish and milky aspect and reducing the transparency, which is detrimental for the use of such surfaces in screens. To avoid the mentioned effect, a thin polymer coating can be used to encapsulate the NP nanostructures, thus reducing the surface scattering. A significant haze reduction is possible when the refractive index of the polymer matches that of the FS substrate in the visible optical range. Moreover, the molecular vibrations of the polymer in the mid-IR region increase the IR emissivity where the NP SPhP cannot be excited. In our case, we chose a poly(methyl methacrylate) (PMMA) coating whose refractive index $n \approx 1.48$.

In our case, a PMMA coating thickness of 1.5 μm on the nanostructures was chosen as a compromise between haze reduction while still preserving the contribution of NPs to the optical response in the mid-IR region.

Figures 3a–c show the effect of PMMA coating on the nanostructured samples. One can see that due to the polymer coating, the haze of the NP samples is removed, allowing high transparency (negligible haze) to the sample. The insets of Figures 3a–c show the measured total transmission and haze (T_{Tot} = 93.1% and H = 0.04% for bare FS). In addition, Figure 3d shows the measured optical response of bare FS and FS +NP before and after PMMA coating in the visible/near-IR optical range. The spectral feature that appears around 900 nm is due to a change of detector in the spectrometer. The PMMA coating on the bare FS produces a small periodic oscillation along the spectra due to small cavity effect between the interlayers.[37] Also, the overall reflection of the sample is increased by about 1%; meanwhile, the overall transmission remains unchanged, which translates to an absorption reduction of the sample. Note that without the coating the FS+NP surface direct T and R near the UV range are reduced to 20% and 0%, respectively (see the Supporting Information). When the coating is added, almost the same R and T than the coated FS surface are obtained due to the reduction of surface scattering.

Figure 3e shows the mid-IR absorption of the different surfaces considered (FS+NP with and without PMMA coating) as compared with the bare FS substrate. On the left panel, the mid-IR absorption of the 1.5 μm PMMA coating on FS is reported, where characteristic vibrational absorption bands overlapping with the SiO_2 phonons can be distinguished.

https://doi.org/10.1021/acsanm.2c03272
ACS Appl. Nano Mater. 2022, 5, 17606–17612

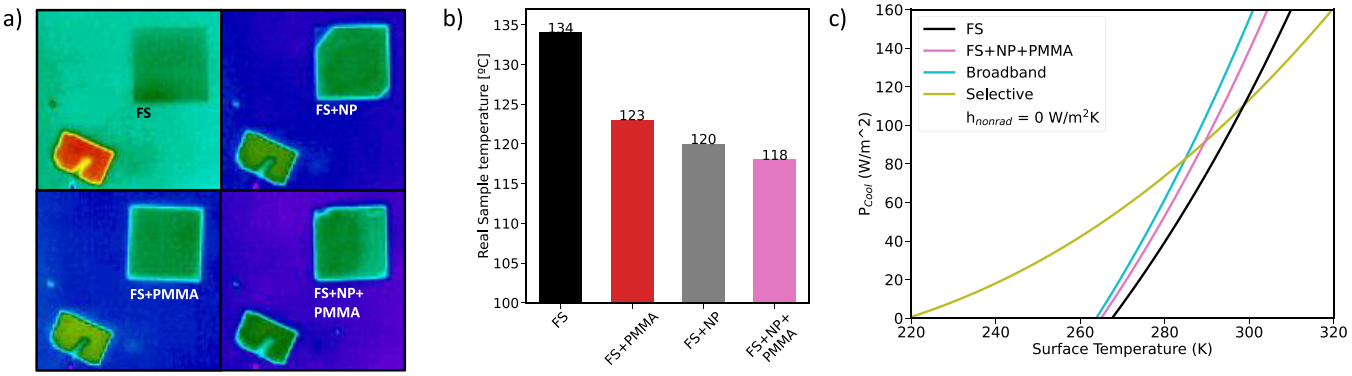

Figure 4. Thermal properties and computed thermal cooling power of the nanostructured surfaces. (a) Thermal camera image of bare FS (top left sample), NP etched on FS (top right sample), bare FS coated with PMMA (bottom left sample), and NP etched on FS and coated with PMMA (bottom right sample) on a hot plate. The temperature of the hot plate is set to a different temperature in each one of the four cases to measure the same "apparent" temperature of the four samples (100 °C). (b) Measured surface temperature for the different samples in (a) showing that the nanostructured samples need less heat from the hot plate, i.e., energy, to extract the same energy than the bare FS. (c) Computed cooling power for the FS and NP+PMMA cases. In blue and green, two theoretical cases of emissivities: a broadband emitter (ε = 1 for λ > 4 μm, blue) and a selective emitter (ε = 1 for λ = 8−13 μm, green). Ambient temperature set at 300 K.

In comparison, the effect of the FS+NP structure is shown in the central panel (red line). Here one can see that the absorption of FS with NP is higher than the PMMA-coated FS for wavelengths lower than ≈9.3 μm due to strong SPhP resonance. However, the coating improves the absorption of the surface when the SPhP cannot be excited due to molecular vibrations. Lastly, the right panel of Figure 3e shows the FS +NP surface coated with PMMA (pink line), resulting in the higher absorption in the mid-IR optical range. In each one of the panels the average absorption in the ATW of the nanostructured surfaces is shown, being ≈0.801 for bare FS. Mid-IR absorption measurements and averaged values in the ATW at different angles of incidence and detection are reported in the Supporting Information.

Finally, to evaluate the proposed nanostructures for radiative cooling applications, we have directly measured the thermal radiation emitted from different samples and related it to the IR optical properties studied above.

In Figure 4a, individual thermal camera images of bare FS and a surface with NP with and without PMMA coating on a hot plate are shown. Because each surface has a different emissivity, the hot plate has to be set to different temperature in each of the four cases to achieve the same "apparent" temperature (100 °C; see Figure 4b). These results are consistent with the trend observed when the hot plate temperature was set the same for all samples, thus confirming the difference in surface emissivity (see the Supporting Information).

To relate these thermal measurements with the optical measurements of Figure 3e, one can use Stefan−Boltzmann's radiation law, $E \propto \varepsilon T^4$, where E is the radiated power emitted by the body at temperature T with emissivity ε, (absorptivity because of Kirchhoff's law). From the calculations reported in the Supporting Information, we confirm that the temperature ratios between the modified surfaces (FS+NP, FS+PMMA, and FS+NP+PMMA) and the bare surface (FS) have similar values as the corresponding average absorption ratios in the working optical range of the thermal camera, as expected from optical characterization.

Figure 4c shows the calculated theoretical cooling power for the FS and the FS+NP+PMMA samples using equations from the literature. For the computation, mid-IR spectral absorption measurements at different angles of illumination and detection were used (see the Supporting Information). In addition, two theoretical cases of emissivities, a broadband emitter (ε = 1 for λ > 4 μm, cyan line) and a selective emitter (ε = 1 for λ = 8−13 μm, green line), are added to compare with literature. More details about the radiative cooling calculations, the effect of the nonradiative contribution, and the comparison with previous studies can be found in the Supporting Information. One can see that the cooling power of the modified sample is higher than that the bare FS, the coated FS+NP sample being the one with higher cooling power for higher temperature, as expected from the experiment in Figure 4a.

CONCLUSIONS

In conclusion, we demonstrated a new nanostructured transparent surface for radiative cooling applications based on lithography-free, scalable fabrication of NPs on glass. The nanostructure reduces the IR reflectivity of the SiO_2 Rest-strahlen band around 9 μm by coupling light into localized SPhP modes. In addition, we showed that coating the nanostructured glass with a thin PMMA removes the haze produced by the NPs in the visible range, resulting in a fully transparent surface suitable for optical displays applications. Lastly, we experimentally verified that our nanostructured surface can extract more heat via radiation, showing an apparent temperature several degrees lower than the bare glass substrate.

ASSOCIATED CONTENT

Supporting Information

The Supporting Information is available free of charge at https://pubs.acs.org/doi/10.1021/acsanm.2c03272.

SEM image and diameter distribution of nanopillars on glass sample; finite element method simulations results of nanopillar array; more visible and near-infrared optical characterization for the fabricated samples; tilted infrared absorption measurements for the fabricated samples; thermal images of the samples in a hot plate at the same temperature, relation between emissivities and sample temperature, radiative cooling power equations, atmospheric and solar data used for radiative cooling

https://doi.org/10.1021/acsanm.2c03272
ACS Appl. Nano Mater. 2022, 5, 17606−17612

power calculations, calculated cooling power with and without nonradiative contributions, resume table with literature results (PDF)

AUTHOR INFORMATION

Corresponding Authors

Bruno Paulillo − *ICFO-Institut de Ciencies Fotoniques, The Barcelona Institute of Science and Technology, 08860 Barcelona, Spain;* orcid.org/0000-0002-6675-0141; Email: bruno.paulillo@icfo.eu

Valerio Pruneri − *ICFO-Institut de Ciencies Fotoniques, The Barcelona Institute of Science and Technology, 08860 Barcelona, Spain; ICREA-Institució Catalana de Recerca i Estudis Avançats, 08010 Barcelona, Spain;* Email: valerio.pruneri@icfo.eu

Authors

Javier Arrés Chillón − *ICFO-Institut de Ciencies Fotoniques, The Barcelona Institute of Science and Technology, 08860 Barcelona, Spain*

Prantik Mazumder − *Corning Research and Development Corporation, Corning, New York 14831, United States*

Complete contact information is available at: https://pubs.acs.org/10.1021/acsanm.2c03272

Notes

The authors declare no competing financial interest.

ACKNOWLEDGMENTS

The authors acknowledge financial support from the Spanish Ministry of Economy and Competitiveness through the "Severo Ochoa" Programme for Centres of Excellence in R&D (CEX2019-000910-S) [MCIN/AEI/10.13039/501100011033] and the project TUNA-SURF (PID2019-106892RB-I00), from Fundació Privada Cellex, Fundació Mir-Puig, and from Generalitat de Catalunya through the CERCA programme, from AGAUR 2017 SGR 1634. This project received funding from the European Union's Horizon 2020 Research and Innovation Programme under the Marie Skłodowska-Curie grant agreement no. 754510 and the "Presidencia de la Agencia Estatal de Investigación" within the "Convocatoria de tramitación anticipada", correspondiente al año 2017, de las ayudas para contratos predoctorales (ref BES-2017-082781) para la formación de doctores contemplada en el Subprograma Estatal de Formación del Programa Estatal de Promoción del Talento y su Empleabilidad en I+D+i, en el marco del Plan Estatal de Investigación Científica y Técnica y de Innovación 2017-2020, cofinanciado por el Fondos Social Europeo.

REFERENCES

(1) Delmastro, C.. *Cooling*. IEA, 2021, Cooling, IEA: Paris,https://www.iea.org/reports/cooling.

(2) Goldstein, E. A.; Raman, A. P.; Fan, S. Sub-Ambient Non-Evaporative Fluid Cooling with the Sky. *Nature Energy* **2017**, *2* (9), 1−7.

(3) Bhamare, D. K.; Rathod, M. K.; Banerjee, J. Passive Cooling Techniques for Building and Their Applicability in Different Climatic Zones—The State of Art. *Energy Build* **2019**, *198*, 467−490.

(4) Munday, J. N. Tackling Climate Change through Radiative Cooling. *Joule* **2019**, *3* (9), 2057−2060.

(5) Rephaeli, E.; Raman, A.; Fan, S. Ultrabroadband Photonic Structures to Achieve High-Performance Daytime Radiative Cooling. *Nano Lett.* **2013**, *13* (4), 1457−1461.

(6) Raman, A. P.; Anoma, M. A.; Zhu, L.; Rephaeli, E.; Fan, S. Passive Radiative Cooling below Ambient Air Temperature under Direct Sunlight. *Nature 2014 515:7528* **2014**, *515* (7528), 540−544.

(7) Hossain, M. M.; Jia, B.; Gu, M. A Metamaterial Emitter for Highly Efficient Radiative Cooling. *Adv. Opt Mater.* **2015**, *3* (8), 1047−1051.

(8) Yuan, H.; Yang, C.; Zheng, X.; Mu, W.; Wang, Z.; Yuan, W.; Zhang, Y.; Chen, C.; Liu, X. U.; Shen, A. W. Effective, Angle-Independent Radiative Cooler Based on One-Dimensional Photonic Crystal. *Optics Express* **2018**, *26* (21), 27885−27893.

(9) Zhu, Y.; Wang, D.; Fang, C.; He, P.; Ye, Y. H. A Multilayer Emitter Close to Ideal Solar Reflectance for Efficient Daytime Radiative Cooling. *Polymers 2019, Vol. 11, Page 1203* **2019**, *11* (7), 1203.

(10) Kim, M.; Lee, D.; Son, S.; Yang, Y.; Lee, H.; Rho, J. Visibly Transparent Radiative Cooler under Direct Sunlight. *Adv. Opt Mater.* **2021**, *9* (13), 2002226.

(11) Dahan, N.; Niv, A.; Biener, G.; Kleiner, V.; Hasman, E. Space-Variant Polarization Manipulation of a Thermal Emission by a SiO_2 Subwavelength Grating Supporting Surface Phonon-Polaritons. *Appl. Phys. Lett.* **2005**, *86* (19), 191102.

(12) Zhu, L.; Raman, A. P.; Fan, S. Radiative Cooling of Solar Absorbers Using a Visibly Transparent Photonic Crystal Thermal Blackbody. *Proc. Natl. Acad. Sci. U. S. A.* **2015**, *112* (40), 12282−12287.

(13) Blandre, E.; Drévillon, J.; Joulain, K.; Yalçin, R. A. Micro-structured Surfaces for Colored and Non-Colored Sky Radiative Cooling. *Optics Express* **2020**, *28* (20), 29703−29713.

(14) Jaramillo-Fernandez, J.; Whitworth, G. L.; Pariente, J. A.; Blanco, A.; Garcia, P. D.; Lopez, C.; Sotomayor-Torres, C. M. A Self-Assembled 2D Thermofunctional Material for Radiative Cooling. *Small* **2019**, *15* (52), 1905290.

(15) Gentle, A. R.; Smith, G. B. Radiative Heat Pumping from the Earth Using Surface Phonon Resonant Nanoparticles. *Nano Lett.* **2010**, *10* (2), 373−379.

(16) Zhai, Y.; Ma, Y.; David, S. N.; Zhao, D.; Lou, R.; Tan, G.; Yang, R.; Yin, X. Scalable-Manufactured Randomized Glass-Polymer Hybrid Metamaterial for Daytime Radiative Cooling. *Science (1979)* **2017**, *355* (6329), 1062−1066.

(17) Chen, D.; Dong, J.; Yang, J.; Hua, Y.; Li, G.; Guo, C.; Xie, C.; Liu, M.; Liu, Q. Realization of Near-Perfect Absorption in the Whole Reststrahlen Band of SiC. *Nanoscale* **2018**, *10* (20), 9450−9454.

(18) Mandal, J.; Fu, Y.; Overvig, A. C.; Jia, M.; Sun, K.; Shi, N. N.; Zhou, H.; Xiao, X.; Yu, N.; Yang, Y. Hierarchically Porous Polymer Coatings for Highly Efficient Passive Daytime Radiative Cooling. *Science (1979)* **2018**, *362* (6412), 315−319.

(19) Fu, Y.; Yang, J.; Su, Y. S.; Du, W.; Ma, Y. G. Daytime Passive Radiative Cooler Using Porous Alumina. *Sol. Energy Mater. Sol. Cells* **2019**, *191*, 50−54.

(20) Zahir, M.; Benlattar, M. Daytime Radiative Cooler Using Porous TiO_2: New Approach. *Applied Optics* **2020**, *59* (30), 9400−9408.

(21) Wang, T.; Wu, Y.; Shi, L.; Hu, X.; Chen, M.; Wu, L. A Structural Polymer for Highly Efficient All-Day Passive Radiative Cooling. *Nat. Commun.* **2021**, *12* (1), 1−11.

(22) Son, S.; Liu, Y.; Chae, D.; Lee, H. Cross-Linked Porous Polymeric Coating without a Metal-Reflective Layer for Sub-Ambient Radiative Cooling. *ACS Appl. Mater. Interfaces* **2020**, *12* (52), 57832−57839.

(23) Lee, D.; Go, M.; Son, S.; Kim, M.; Badloe, T.; Lee, H.; Kim, J. K.; Rho, J. Sub-Ambient Daytime Radiative Cooling by Silica-Coated Porous Anodic Aluminum Oxide. *Nano Energy* **2021**, *79*, 105426.

(24) Li, X.; Peoples, J.; Huang, Z.; Zhao, Z.; Qiu, J.; Ruan, X. Full Daytime Sub-Ambient Radiative Cooling in Commercial-like Paints with High Figure of Merit. *Cell Rep. Phys. Sci.* **2020**, *1* (10), 100221.

(25) Chae, D.; Son, S.; Lim, H.; Jung, P. H.; Ha, J.; Lee, H. Scalable and Paint-Format Microparticle−Polymer Composite Enabling High-Performance Daytime Radiative Cooling. *Materials Today Physics* **2021**, *18*, 100389.
(26) Ziming, C.; Fuqiang, W.; Dayang, G.; Huaxu, L.; Yong, S. Low-Cost Radiative Cooling Blade Coating with Ultrahigh Visible Light Transmittance and Emission within an "Atmospheric Window. *Sol. Energy Mater. Sol. Cells* **2020**, *213*, 110563.
(27) Kou, J.; Jurado, Z.; Chen, Z.; Fan, S.; Minnich, A. J. Daytime Radiative Cooling Using Near-Black Infrared Emitters. *ACS Photonics* **2017**, *4* (3), 626−630.
(28) Nicholas, B.; Gregory, B.; Wageesha, S.; Sergey, T. System for solar heating mitigation, WO2019/140092A1.
(29) Wang, S.; Zhou, Y.; Jiang, T.; Yang, R.; Tan, G.; Long, Y. Thermochromic Smart Windows with Highly Regulated Radiative Cooling and Solar Transmission. *Nano Energy* **2021**, *89*, 106440.
(30) Kitamura, R.; Pilon, L.; Jonasz, M. Optical Constants of Silica Glass from Extreme Ultraviolet to Far Infrared at near room Temperature. *Applied Optics* **2007**, *46* (33), 8118−8133.
(31) Wang, T. B.; Liu, Z. G.; Tan, C. Z. Relationship between the Frequency of the Main LO Mode of Silica Glass and Angle of Incidence. *J. Chem. Phys.* **2003**, *119* (1), 505.
(32) Fox, M. *Optical Properties of Solids*, 2nd ed.; OUP: Oxford, 2010; Vol. *3*.
(33) Rombaut, J.; Martínez, S.; Matera, U. M.; Mazumder, P.; Pruneri, V. Antireflective Multilayer Surface with Self-Cleaning Subwavelength Structures. *ACS Photonics* **2021**, *8*, 894−900.
(34) Infante, D.; Koch, K. W.; Mazumder, P.; Tian, L.; Carrilero, A.; Tulli, D.; Baker, D.; Pruneri, V. Durable, Superhydrophobic, Antireflection, and Low Haze Glass Surfaces Using Scalable Metal Dewetting Nanostructuring. *Nano Research 2013 6:6* **2013**, *6* (6), 429−440.
(35) Gemini Observatory. IR Transmission Spectra, Gemini Observatory Kernel Description. http://www.gemini.edu/?q/node/10789 (accessed 2021-01-05).
(36) Marquier, F.; Greffet, J.-J.; Joulain, K. Resonant Infrared Transmission through SiC Films. *Optics Letters* **2004**, *29* (18), 2178−2180.
(37) Yang, Q.; Zhang, X. A.; Bagal, A.; Guo, W.; Chang, C. H. Antireflection Effects at Nanostructured Material Interfaces and the Suppression of Thin-Film Interference. *Nanotechnology* **2013**, *24* (23), 235202.

https://doi.org/10.1021/acsanm.2c03272
ACS Appl. Nano Mater. 2022, 5, 17606−17612